

Critical current vs. magnetic field dependence in ramp-zigzag Josephson junctions

S. Scharinger,¹ M. Turad,¹ A. Stöhr,¹ V. Leca,^{1,2} E. Goldobin,¹ R. G. Mints,³ D. Koelle,¹ and R. Kleiner^{1,*}

¹*Physikalisches Institut and Center for Collective Quantum Phenomena in LISA⁺,
Universität Tübingen, Auf der Morgenstelle 14, D-72076, Tübingen, Germany*

²*National Institute for Research and Development in Microtechnologies,*

Molecular Nanotechnology Laboratory, Erou Iancu Nicolae Str. 126A, RO-077190, Bucharest, Romania

³*The Raymond and Beverly Sackler School of Physics and Astronomy, Tel Aviv University, Tel Aviv 69978, Israel*

(Dated: December 8, 2018)

We study the critical current I_c dependence on applied magnetic field H for multifacet $\text{YBa}_2\text{Cu}_3\text{O}_{7-\delta}$ -Au-Nb zigzag Josephson junctions. For many experiments one would like to apply a homogeneous field parallel to the junction plane. However, even tiny misalignments can cause drastic deviations from homogeneity. We show this explicitly by measuring and analyzing I_c vs. H for an 8 facet junction, forming an array of $4 \times (0-\pi)$ -segments. H is applied under different angles θ relative to the substrate plane and different angles ϕ relative to the in-plane orientation of the zigzags. We find that even a small misalignment $\theta \sim 0.2^\circ$ can cause a substantial inhomogeneity of the flux density inside the junction, drastically altering its I_c vs. H interference pattern. We also show, that there is a dead angle θ_d of similar magnitude, where the average flux density completely vanishes.

PACS numbers: 74.50.+r, 85.25.Cp, 74.78.Fk

A. Introduction

Large (in a geometrical sense) Josephson junctions (JJs) are studied intensively since decades, *e.g.* in the context of Josephson fluxon physics. Interesting and important physics is related to junctions where some regions obey the usual Josephson relation, while other regions incorporate an additional phase jump of π , which can be viewed as a negative critical supercurrent density $j_c < 0$. These $0-\pi$ junctions can be fabricated in different ways, *e.g.* by connecting a d wave superconductor such as $\text{YBa}_2\text{Cu}_3\text{O}_{7-\delta}$ (YBCO)¹⁻⁴ or $\text{Nd}_{2-x}\text{Ce}_x\text{CuO}_{4-\delta}$ (NCCO)^{4,5} to a conventional superconductor like Pb or Nb, or by using biepitaxial grainboundaries in YBCO^{6,7}, superconductor-ferromagnet-superconductor (SFS) or superconductor-insulator-ferromagnet-superconductor junctions (SIFS)⁸⁻¹⁰. In the YBCO-Nb or NCCO-Nb structures the Josephson junction is often of the ramp type and the barrier forms a zigzag line parallel to the crystallographic a and b axes²⁻⁵, see Fig. 1. This type of junction has been important for determining the symmetry of the order parameter of the cuprate superconductors^{1,11}.

In addition, several properties make zigzag junctions very interesting for ongoing studies. In particular, half-integer vortices (semifluxons) can form spontaneously at the corners of the zigzag line and, thus, quasi-one-dimensional vortex crystals can be realized^{3,12}. Also, under special conditions the zigzag junctions can be used to create φ_0 ^{13,14} or φ junctions, with an arbitrary value of the ground state phase φ ¹⁵⁻¹⁸. Such junctions, if long compared to the Josephson penetration depth λ_J , can carry mobile fractional vortices (splintered vortices) having many unusual properties^{16,19-22}. Apart from these research areas, aiming mostly at long junctions, ramp

junctions are also interesting for superconducting electronics, *e.g.* in the context of self-biased RSFQ circuits²³ or in the context of superconducting quantum interference filters^{24,25}. In all cases a good understanding of the implications of the zigzag ramp geometry is required.

Studies of semifluxons or splintered vortices in many cases require the application of a magnetic field which, in theoretical studies, is usually considered to be oriented parallel to the junction plane. Experimental studies on the zigzag junctions have usually been performed with the magnetic field applied perpendicular to the substrate plane²⁻⁵. One reason for this was the finding that, when aligning the substrate parallel to the magnetic field, apart from a field scaling factor due to flux focusing, no essential difference to the perpendicular field orientation was observed. Theoretical interference patterns I_c vs. H , calculated for a homogeneous field applied parallel to the junction plane, and the experimental patterns agreed only qualitatively: the critical current I_c was maximum when the flux per $(0-\pi)$ -segment roughly equalled one flux quantum²⁻⁵. However, in almost any other respect experimental and theoretical I_c vs. H curves were not even similar.

It was shown previously that for a perpendicular field orientation the flux density B in the junction barrier becomes inhomogeneous even in the case of a homogeneous applied field H ²⁶⁻³⁰, leading, *e.g.*, to a striking difference of I_c vs. H for SIFS multifacet $0-\pi$ junctions (SIFS-MJJs), when measured in parallel, and perpendicular fields, respectively^{29,31}. Moreover, for H applied under an angle θ relative to the substrate plane there is a “dead angle” θ_d where the magnetic flux caused by the parallel ($\theta = 0^\circ$) and perpendicular ($\theta = 90^\circ$) components (H_{\parallel} and H_{\perp} , respectively) of H cancel, leading to a critical current which almost does not modulate with H ^{27,29,32}.

The dead angle θ_d can be very close to zero, making proper junction alignment parallel to H very difficult, if not impossible.

However, ramp zigzag junctions are considerably more complex than conventional overlap junctions or SIFS-MJJs and need separate consideration. A systematic study under oblique fields seems necessary, having in mind that this type of junction is very useful for many future investigations. In the present study we have chosen a $\text{YBa}_2\text{Cu}_3\text{O}_7$ -Au-Nb junction with 8 facets ($4 \times (0-\pi)$ -segments), each facet being $10\ \mu\text{m}$ long. We have investigated its $I_c(H)$ dependence as a function of θ and also the in-plane angle ϕ , where $\phi = 0^\circ$ corresponds to H_{\parallel} applied parallel to one of the facets. It turns out that H_{\perp} leads to a periodically modulated flux density profile. Its average value is enormously compressed, by a factor $f \approx 100$ relative to the flux density generated by H_{\parallel} . As a consequence, the dead angle is very small, $\theta_d \approx -0.38^\circ$ for $\phi = 45^\circ$ and $\theta_d \approx -0.25^\circ$ for $\phi = 0^\circ$. To achieve a more or less homogeneous flux density B , the field H must be aligned better than some 0.1° relative to $\theta = 0^\circ$ and, to achieve $1\ \Phi_0$ or more per $(0-\pi)$ -segment, $\mu_0 H$ values of more than 3 mT are required. These conditions require quite dedicated experimental setups. Alternatively, realistic theoretical analyses should be based on the case of $\theta = 90^\circ$.

B. Samples and Measurement Techniques

The YBCO layer was grown by pulsed laser deposition (PLD) on a [001]-oriented SrTiO_3 single crystal substrate. The substrate temperature T_s during the deposition of the 65 nm thick YBCO thin films was 770°C and the oxygen pressure P_{O_2} was 20 Pa. A 60 nm thick SrTiO_3 insulation layer on top of YBCO was also deposited by PLD at $T_s = 760^\circ\text{C}$ and $P_{\text{O}_2} = 9$ Pa. The targets were ablated using a KrF excimer laser at a repetition rate of 2 Hz. After thin film deposition, the chamber was vented with oxygen up to 0.5 bar and the sample was cooled down to room temperature, with an annealing step at 450°C for 30 min. The zero-resistance transition temperatures T_c of the YBCO films were between 88 and 90 K. The YBCO/ SrTiO_3 bilayer was patterned using optical lithography and Ar-ion milling under an angle of 30° between surface normal and ion beam. To ensure a constant ramp angle for all junction orientations the sample was rotated about the axis normal to the surface during milling. With these parameters a ramp angle of $\theta_r = 8^\circ$ was obtained. After removal of the photoresist and before the next deposition steps, the sample surface was cleaned in a soft Ar rf-plasma. Another 4 unit cells of YBCO were grown by PLD with the same deposition and annealing parameters as before to provide recrystallization³³. With electron beam evaporation a 9 nm Au barrier was deposited, followed by a sputtered Nb layer of thickness $d_{\text{Nb}} = 100$ nm. The plasma-cleaning and the last three depositions steps were done without

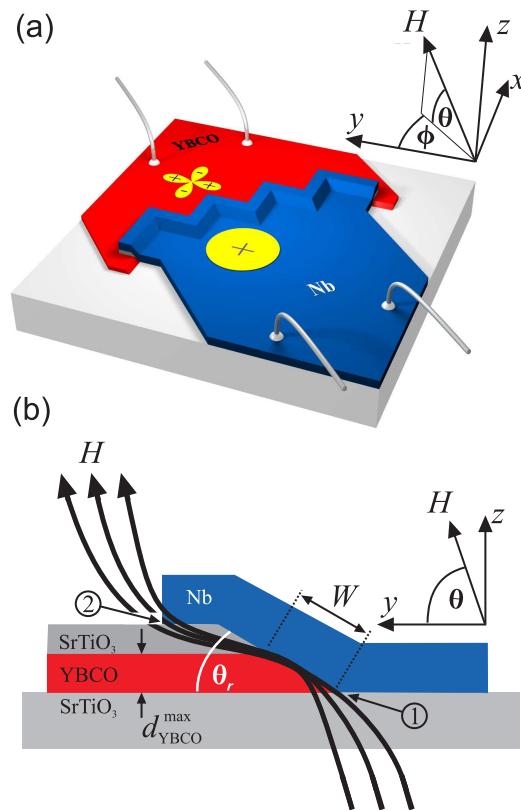


FIG. 1: (Color online). Sketch of ramp zigzag junction: (a) whole junction with 8 facets, (b) cross section of one facet. Penetration and focusing effect of applied magnetic field along the ramp are indicated by black lines. Coordinates and ramp angle θ_r , as used in sections C and D, as well as angles θ and ϕ of applied field are indicated.

breaking the vacuum. The Nb and Au layer were patterned by a final photo lithography and Ar-ion milling step. An example of the JJ is sketched in Fig. 1.

The samples were measured at $T = 4.2$ K in a magnetically and electrically shielded cryostat. The mounted sample typically had a misalignment of the applied magnetic field relative to the substrate plane θ_{off} below 1° . An external field $\mu_0 H$ of up to 3.5 mT could be applied and continuously rotated with respect to θ via two perpendicular coils operated in linear combination and creating $H_{\parallel} = H \cos \theta$ and $H_{\perp} = H \sin \theta$. The in-plane angle ϕ was varied by mounting the sample with proper orientation relative to the in-plane field axis, resulting in a misalignment error $\phi_{\text{off}} \sim 2 - 3^\circ$.

Below we discuss results from our most homogeneous sample. Fig. 2 shows current voltage characteristics, measured at three values of applied field. The current voltage characteristics were hysteretic for critical currents $> 2\ \mu\text{A}$, with a junction resistance of $R \approx 6.6\ \Omega$. To measure I_c the bias current I was ramped up at fixed magnetic field until the junction switched to its resistive state. A voltage criterion $V_{\text{cr}} = 2\ \mu\text{V}$ was used to deter-

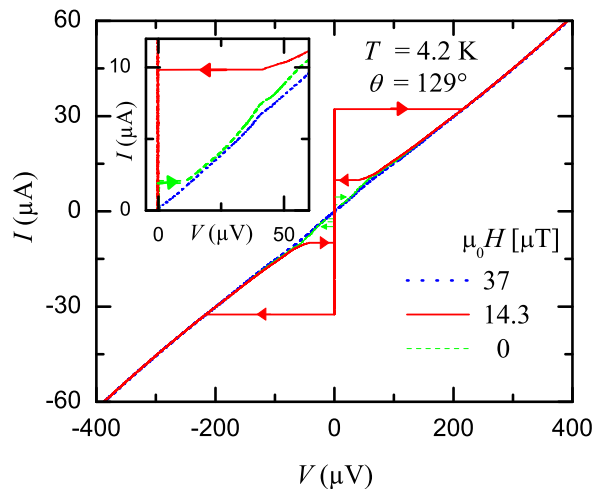


FIG. 2: (Color online). Current voltage characteristic of the 8-facet ramp zigzag JJ at $T = 4.2$ K for 3 different values of magnetic field, applied at $\theta = 129^\circ$: $14.3 \mu\text{T}$ (main I_c maximum), $0 \mu\text{T}$ and $37 \mu\text{T}$ (I_c minimum). Inset shows current voltage characteristic at expanded scales.

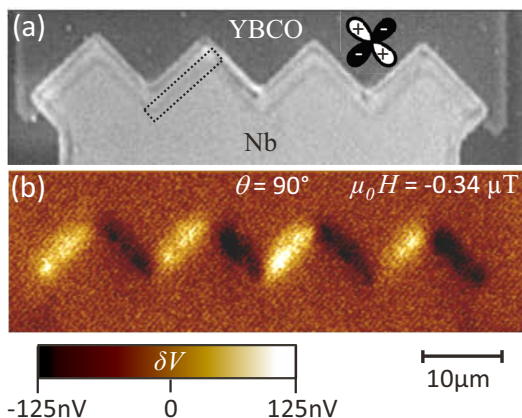


FIG. 3: (Color online) Images of the 8-facet YBCO-Nb zigzag JJ: (a) SEM surface image. The $d_{x^2-y^2}$ -wave order parameter of the YBCO layer is indicated by the cloverleaf structure. White and black lobes are orientated along the crystallographic a and b axes and indicate the sign change of the order parameter. The dotted rectangle surrounds the ramp area of one facet. (b) LTSEM δV image taken at $T = 8.0$ K, $I = 2.3 \mu\text{A}$ and $\mu_0 H = -0.34 \mu\text{T}$ (central I_c minimum at small offset field for $\theta = 90^\circ$).

mine I_c , leading to a maximum over-estimate of I_c by $V_{\text{cr}}/R \sim 0.3 \mu\text{A}$ in the nonhysteretic regime. In the hysteretic regime I_c is underestimated by some $0.1 \mu\text{A}$ due to premature thermal activation.

Fig. 3 (a) shows a scanning electron microscopy (SEM) surface image of the YBCO-Nb zigzag junction. The dotted rectangle surrounds the ramp area of one facet, which is visible as a faint grey line. The top Nb electrode overlaps the YBCO ramp area by extra $3 \mu\text{m}$ (idle region).

The ramp areas of all facets form a zigzag line parallel to the a, b axes of the YBCO film.

To investigate the homogeneity of the critical current densities of individual facets j_c^i , we have imaged the current distribution of the entire zigzag junction at zero magnetic flux using low temperature scanning electron microscopy (LTSEM). Details of the method can be found in Ref. 4. In brief, the pulsed focused electron beam, which is scanned across the sample, causes local heating $\delta T < 1$ K on a lateral length scale of $\approx 1\text{-}3 \mu\text{m}$, which determines the spatial resolution of this imaging technique. The measured integral quantity is the voltage V across the junction, which is biased slightly above I_c . δT results in a local reduction of $|j_c(T)|$. The corresponding change of the overall I_c of the zigzag junction causes a slight change of $\delta V(x, y)$, which depends on the beam position (x, y) on the sample surface. For a bias current slightly above I_c and $B = 0$, $\delta V(x, y) \propto -j_c(x, y)$. This imaging technique requires non-hysteretic current-voltage characteristics, which for our junction is not the case for $T = 4.2$ K, cf. Fig. 2. Therefore, the $\delta V(x, y)$ image of the YBCO-Nb zigzag junction in Fig. 3 (b) has been taken at $T = 8.0$ K. The junction has been biased at $I = 2.3 \mu\text{A}$. A field $\mu_0 H = -0.34 \mu\text{T}$ was applied to compensate the residual field in the LTSEM setup. The δV image clearly shows the alternating sign of supercurrent flow across neighboring facets. On the scale of the spatial resolution of our imaging technique neither defects nor j_c asymmetries between facets are visible. Furthermore, the critical current densities of the facets seems to be quite homogeneous.

C. General Considerations

1. Single-Facet Ramp Junction

Before we address $I_c(H)$ of zigzag JJs let us first theoretically consider a JJ with a single facet oriented parallel to the x axis, see Fig. 1 (b). The facet starts at $(x, y) = 0$ and extends to a length L along the x direction. The bottom YBCO electrode grows in thickness along y , reaching its maximum thickness $d_{\text{YBCO}}^{\text{max}} = 65$ nm at $y = d_{\text{YBCO}}^{\text{max}}/\tan(\theta_r) = 462$ nm, which is the projection of the junction width $W = d_{\text{YBCO}}^{\text{max}}/\sin(\theta_r) = 467$ nm to the y axis. H shall be oriented in y direction ($\phi = 0^\circ$). Since $d_{\text{YBCO}}^{\text{max}}$ is well below the YBCO in-plane magnetic penetration depth $\lambda_{\text{YBCO}} \sim 150$ nm, the flux density B for H oriented parallel to the substrate plane ($\theta = 0^\circ$) is almost homogeneous and equal to $\mu_0 H$ inside the YBCO film.

When H is applied perpendicular to the substrate plane ($\theta = 90^\circ$) screening currents in the superconducting electrodes, preventing magnetic field lines from crossing the superconducting layers, lead to a strongly enhanced flux density in the junction barrier cf. Fig. 1 (b). For a magnetic field applied *perpendicular* to the junction plane the effective penetration depth (Pearl length)

is $\Lambda = \lambda_{\text{YBCO}}^2/d_{\text{YBCO}} > 350 \text{ nm}$. Thus, over the junction area the magnetic flux can penetrate almost completely in the YBCO film. The thickness of the Nb film is comparable to the respective penetration depth ($\lambda_{\text{Nb}} \sim 80 \text{ nm}$) and approximately constant over the ramp area. We may represent the resulting flux density profile inside the junction barrier, for the component oriented along $\theta = \theta_r$, as $B_{90,f}(x) = \mu_0 H_{\perp} f_{90,f} N_{90,f} [a_{90,f} + P_{90,f}(x)]$, where the field compression factor $f_{90,f} \gg 1$. The normalization constant $N_{90,f}$ is chosen such that the spatial average of $N_{90,f}(a_{90,f} + P_{90,f}(x))$ equals 1. The index ‘90’ indicates perpendicular direction of the applied field and subscript ‘f’ indicates the single facet scenario. The spatially dependent field profile $P_{90,f}(x) > 0$, to be specified later, is maximum in the center of the junction and is assumed to reach zero at its edges. Without idle regions $B_{90,f}$ would drop to almost zero at the junction edges, *i.e.* $a_{90,f} \approx 0$. The effect of the idle regions is to make $B_{90,f}$ nonzero here. This is parametrized by $a_{90,f}$. Using the spatial average $\langle P_{90,f} \rangle$ of $P_{90,f}(x)$, $B_{90,f}$ can be regrouped as

$$B_{90,f}(x) = \mu_0 H_{\perp} f_{90,f} (1 + \tilde{P}_{90,f}(x)) \equiv H_{\perp} g_{90,f}(x) \quad (1)$$

where $\tilde{P}_{90,f}(x) = N_{90,f}(P_{90,f}(x) - \langle P_{90,f} \rangle)$ has vanishing average.

The case of “parallel” fields requires some discussion. In our coordinate system it means parallel to the substrate plane. For theoretical considerations “parallel” should refer to an angle (relative to the substrate plane) where the flux density in the junction is homogeneous. In the absence of idle regions a natural choice would be the ramp plane, *i.e.*, H applied at $\theta = \theta_r$. Screening currents in the idle regions, however, will deform the flux density similar to the case of perpendicular fields, leading to an ambiguity of what “parallel” actually means.

Let us start with a field H applied at $\theta = 0^\circ$. Screening currents in the vicinity of the ramp cause B to be (almost) parallel to the Nb film, *i.e.* tilted by θ_r within the area of the YBCO ramp. These screening currents also cause a slight field compression towards the center of the ramp. For the case of $\theta = 0^\circ$ we thus expect a flux density profile for the component along θ_r of the form $B_{0,f}(x) = \mu_0 H_{\parallel} f_{0,f} N_{0,f} [a_{0,f} + P_{0,f}(x)]$, where the subscript ‘0’ stands for $\theta = 0^\circ$. $f_{0,f} \gtrsim 1$ represents field compression. $N_{0,f}$ normalizes the field profile to 1. $P_{0,f}(x)$ has an absolute value which is maximum in the center of the facet and zero at its edges. The constant $a_{0,f}$ has been introduced to account for idle region effects.

By decomposing H_{\parallel} into components perpendicular and parallel to the ramp one realizes that $P_{0,f} \leq 0$ at least in the absence of idle regions. The screening currents in the idle regions reduce $|P_{0,f}(x)|$.

Similar as $B_{90,f}$, $B_{0,f}(x)$ can be regrouped as

$$B_{0,f}(x) = \mu_0 H_{\parallel} f_{0,f} (1 + \tilde{P}_{0,f}(x)) \equiv H_{\parallel} g_{0,f}(x) \quad (2)$$

where $\tilde{P}_{0,f}(x) = N_{0,f}(P_{0,f}(x) - \langle P_{0,f} \rangle)$ has vanishing average.

If H is oriented within the (y, z) plane at an arbitrary angle θ relative to the y axis the total flux density in the junction is $B_f(x) = H \cos(\theta) g_{0,f}(x) + H \sin(\theta) g_{90,f}(x)$. If the spatial dependences of $\tilde{P}_{0,f}(x)$ and $\tilde{P}_{90,f}(x)$ are similar, the ratio $p = |\tilde{P}_{0,f}/\tilde{P}_{90,f}|$ is about constant. Then, there is an angle $\theta_h = -\arctan(f_{0,f}p/f_{90,f})$ where the field penetrating the junction is homogeneous and given by $B_{h,f} = \mu_0 H \cos \theta_h f_{0,f}(1 - p)$. The angle θ_h might be referred to as “field applied parallel to the ramp plane”³². In the absence of idle regions we expect $\theta_h \approx \theta_r$. In their presence θ_h is reduced. We did not perform an explicit calculation, but a guess is to consider a field line, which starts at the YBCO ramp edge [point ① in Fig. 1 (b)] and touches the edge of the overlapping Nb film [point ② in Fig. 1 (b)], which, for $\phi = 45^\circ$ (the relevant angle for the multifacet system), is at the projected length $\tilde{x} \approx 4 \mu\text{m}$ and $z = 125 \text{ nm}$. The corresponding angle is $\theta = 1.8^\circ$.

A similar argument will hold for a multifacet system. In the data shown below we determined the misalignment angle relative to θ_h (“parallel” alignment, homogeneous field) as $\theta_{\text{off}} = 1.68^\circ$ at $\phi = 45^\circ$ and as $\theta_{\text{off}} = 0.85^\circ$ at $\phi = 0^\circ$. Both values are within our experimental accuracy, referring to $\theta = 0^\circ$, but at their extreme. They are fully compatible with the above estimate of θ_h but rule out $\theta_h = \theta_r$.

We further on do not explicitly distinguish θ_h from $\theta = 0^\circ$ and use $f_{0,f} = 1$, $P_{0,f} = 0$ and $N_{0,f} a_{0,f} = 1$.

Another issue arises from the fact that the ramp width W [cf. Fig. 1 (b)] is comparable to the Pearl length. As a consequence, flux lines can leave the junction area and thus the flux through the junction is not conserved. Alternatively, assuming a constant flux density along y , this can be rephrased in terms of an effective junction thickness t_{eff} that varies along the y direction. Generally, t_{eff} can be found via³⁴ $t_{\text{eff}} = t_{\text{Au}} + \lambda_{\text{YBCO}} \tanh(d_{\text{YBCO}}/2\lambda_{\text{YBCO}}) + \lambda_{\text{Nb}} \tanh(d_{\text{Nb}}/2\lambda_{\text{Nb}})$. Over the ramp area, the YBCO film thickness d_{YBCO} grows along y from 0 to $d_{\text{YBCO}}^{\text{max}}$. Thus, t_{eff} increases from $\sim 53 \text{ nm}$ to $\sim 85 \text{ nm}$ over the ramp. For further calculations we use a linearized Ansatz $t_{\text{eff}}(y) = (t_{\text{eff}0} + \Delta t_{\text{eff}} y/W)$, with $-0.5 < y/W < 0.5$.

Ignoring self-field effects caused by the Josephson current, the Josephson phase γ is calculated via

$$\frac{d\gamma(x, y)}{dx} = \frac{2\pi}{\Phi_0} B(x) t_{\text{eff}}(y). \quad (3)$$

The maximum supercurrent is obtained from

$$I_c(H) = \max_{\gamma_0} \left\{ \iint dx dy j_c(x) \sin[\gamma(x, y) - \gamma_0] \right\} \quad (4)$$

where integration has to be performed over the junction area. The dependence of t_{eff} on y causes dephasing, which becomes severe when the flux *difference* (along y) over the junction width becomes on the order of $\Phi_0/2$. In the above estimate t_{eff} differs by $\Delta t_{\text{eff}}/t_{\text{eff}0} \approx 0.5$ from

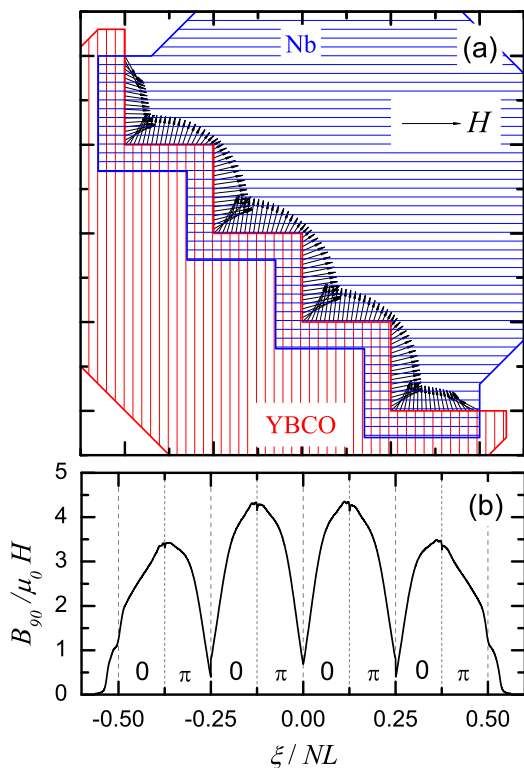


FIG. 4: (Color online). (a) Simulated in-plane field lines (black arrows) between two overlapping planar superconducting layers (YBCO, red vertical lines, Nb, blue horizontal lines) separated by a distance $d_L = 500$ nm. (b) Flux density profile $B_{90}(\xi)$ of the calculated in-plane magnetic field B projected onto the zigzag line.

its average value $t_{\text{eff}0}$ (~ 69 nm), and thus we expect the effect to become noticeable when the total flux through the junction becomes larger than about Φ_0 . However, the data discussed below for the 8 facet junction indicate $\Delta t_{\text{eff}}/t_{\text{eff}0} \approx 0.02$. Also, for $t_{\text{eff}0}$ our data indicate a value which is close to 85 nm, *i.e.* only the “thick” part of the ramp seems to be relevant. The above expression for t_{eff} assumed isotropic superconductors and, thus, the YBCO anisotropy could lead to modifications. Whether or not this solves the discrepancy is unclear to us.

2. Multifacet Ramp Junction

To get an idea of the field focused flux density profile inside the junction for H applied at $\theta = 90^\circ$, we have simulated the flux density distribution around two overlapping planar superconducting layers separated by a distance d_L , using 3D-MSLI³⁵, see hatched areas in Fig. 4 (a). The ramp was not included. The layer shape corresponded to the experimental situation and included $N = 8$ facets of length $L = 10 \mu\text{m}$. We used $d_L = 200$ nm and 500 nm. Smaller values of d_L led to convergence problems. The layer thicknesses were $d_{\text{YBCO}} = 65$ nm

and $d_{\text{Nb}} = 100$ nm, respectively. Fig. 4 (a) shows the calculated geometry and the field lines calculated in the plane parallel to the films and situated in the middle of the $d_L = 500$ nm gap between the films. The field was calculated along the edge of the YBCO film. B is strongest at the inner edges of the YBCO layer and weakest at the outer edges. A flux density profile $B_{90}(\xi)$ of the calculated in-plane magnetic field B projected onto the zigzag line is shown in Fig. 4 (b). ξ is a curvilinear coordinate along the zigzag edge of YBCO. The projection is in units of $\mu_0 H$ and the coordinate ξ runs along the facets, $-0.5 \leq \xi/NL \leq 0.5$. $B_{90}(\xi)/\mu_0 H$ varies roughly sinusoidally, with one period per $(0-\pi)$ -segment (by contrast, one might have expected one period per facet). $B_{90}(\xi)/\mu_0 H$ reaches a maximum value of about 4.5, which is in fact much less than the actual field compression found in experiment ($f_{90} \sim 100$). It also turned out that the B component *perpendicular* to the layers is of the order of the in-plane component – a feature which we expect to disappear in a more realistic scenario. Further, simulating $I_c(H)$ with the profile of Fig. 4 (b) gave strong differences to the experimental interference pattern for flux values larger than Φ_0 per $(0-\pi)$ -segment.

For the simulations discussed below we thus use a more general form for $B_{90}(\xi)$. Each $(0-\pi)$ -segment is described by a field profile $a_{90,f} + P_{90,f}(x)$, with $0 < x < 2L$. We used $P_{90,f}(x) = (\sin(\pi x/2L))^{\alpha_f}$. The resulting periodic pattern along ξ is multiplied by an envelope function $E(\xi) = a_{90,e} + P_{90,e}(\xi)$ extending smoothly across the whole junction. We parametrized $P_{90,e}$ via $(1 - (2\xi/NL)^2)^{\alpha_e}$.

The overall shape of $B_{90}(\xi)$ is given by

$$B_{90}(\xi) = \mu_0 H f_{90} N_{90} [a_{90,e} + P_{90,e}(\xi)] [a_{90,f} + P_{90,f}(\xi)]. \quad (5)$$

N_{90} normalizes the spatial average of $B_{90}/\mu_0 H f_{90}$ to 1.

For arbitrary values of θ and ϕ the flux density B through facets oriented parallel to x is $B_{90}(\xi)\sin\theta + B_0\cos\theta\cos\phi$. For facets oriented parallel to y one obtains $B_{90}(\xi)\sin\theta + B_0\cos\theta\sin\phi$ with a homogeneous flux density $B_0 = B_{h,f} = \mu_0 H$ along the zigzag line. Using this field profile we solved equations Eq. (3) and (4), with x replaced by ξ . The critical current density j_c has been assumed to be constant in amplitude (homogeneous junction). It changes sign between adjacent facets.

D. Results

Fig. 5 (a) compares measured and calculated interference patterns for $\theta = 90^\circ$. The horizontal scales of the calculated patterns are in units of $H_0/f_{90} = NLt_{\text{eff}0}/\Phi_0$. The solid (black) line is for $\Delta t_{\text{eff}}/t_{\text{eff}0} = 0.02$, the dotted (blue) line is for $\Delta t_{\text{eff}} = 0$. The agreement between measured and calculated (for $\Delta t_{\text{eff}}/t_{\text{eff}0} = 0.02$) interference patterns is reasonable, although differences occur for normalized fields $Hf_{90}/H_0 \gtrsim 5$. For $\Delta t_{\text{eff}}/t_{\text{eff}0} > 0.02$, at high fields the I_c maxima are suppressed in comparison

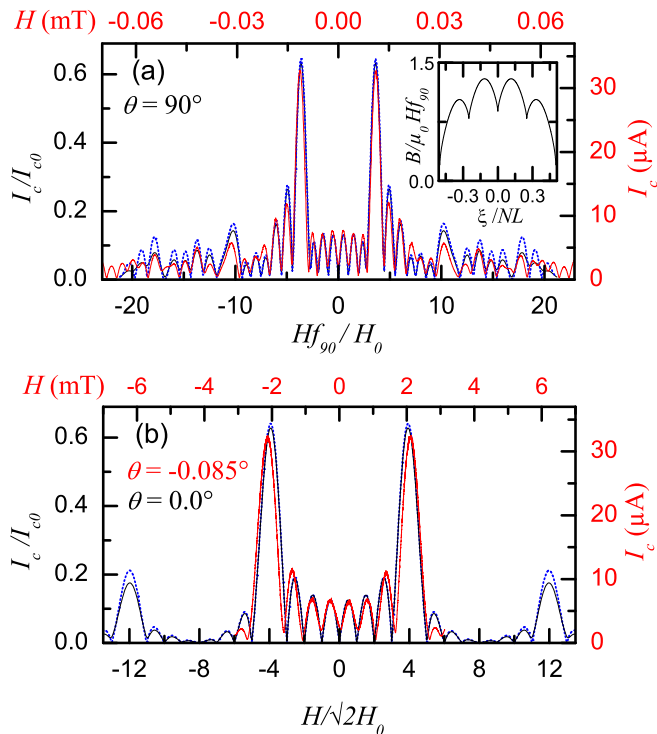


FIG. 5: (Color online). Measured (red) and calculated (black, blue) interference patterns for (a) $\theta = 90^\circ$ and (b) $\phi = 45^\circ$ and $\theta = 0^\circ$ (calculation), $\theta = -0.085^\circ$ (measurement; $\theta_{\text{off}} = 1.684^\circ$ subtracted). Model parameters are $\alpha_e = 0.5$, $a_{90,e} = 0.3$, $\alpha_f = 0.7$, $a_{90,f} = 2.0$, $f_{90} = 100$. For the black curve $\Delta t_{\text{eff}}/t_{\text{eff}0} = 0.02$, for the dotted (blue) line $\Delta t_{\text{eff}} = 0$. $H_0/f_{90} = NLt_{\text{eff}0}/\Phi_0$. Critical current in the calculated plots is normalized to $I_{c0} = |j_c|A_J$, where j_c is the critical current density and A_J is the junction area. Inset in (a) shows flux density profile B_{90} normalized to $\mu_0 H f_{90}$.

with the $\Delta t_{\text{eff}}/t_{\text{eff}0} = 0.02$ case, while the I_c minima are significantly lifted from zero, both in contrast to the measurements. Thus the margin on $\Delta t_{\text{eff}}/t_{\text{eff}0}$ is relatively narrow. For the $(0-\pi)$ -segments we used $\alpha_f = 0.7$ and $a_{90,f} = 2.0$. The power α_f was suggested by the 3D-MSLI simulations. The calculated interference patterns, however did not depend strongly on this parameter. By contrast, the quite large value of $a_{90,f}$ was necessary to achieve a reasonable agreement with experimental data. As a result, the periodic modulations of $B_{90}(\xi)$ are much shallower than suggested by the 3D-MSLI simulations. For the envelope function we used $\alpha_e = 0.5$ and $a_{90,e} = 0.3$. Normalization resulted in $N_{90} = 0.34$. The corresponding field profile is shown in the inset of Fig. 5 (a). Finally, by matching the abscissas of the theoretical and measured interference patterns we find $t_{\text{eff}0}f_{90} = 8.5 \mu\text{m}$. A thickness $t_{\text{eff}0} = 69 \text{ nm}$ calculated from geometry (film thicknesses) corresponds to $f_{90} = 120$. In fact, for the $I_c(H)$ data at different values of θ and ϕ this value turned out to be somewhat too large. Best agreement was obtained for $f_{90} \sim 100$, corresponding to $t_{\text{eff}0} \sim 85 \text{ nm}$.

We mention here that a periodic modulation of $B_{90}(\xi)$ with one period per facet rather than one period per $(0-\pi)$ -segment also gave satisfactory agreement between calculated and measured interference patterns. Thus, from $I_c(H)$ we cannot unambiguously distinguish these scenarios.

Fig. 5 (b) shows measured and calculated interference patterns near parallel orientation ($\theta = \pm 0.1^\circ$) for $\phi = 45^\circ$. For the calculation ($\theta = 0^\circ$) we have assumed that the magnetic flux density along the zigzag line of the multifacet junction $B_0(x)$ is homogeneous, *i.e.* $B_0(x) = \mu_0 H$. The field scale is given in units of $H_0\sqrt{2}$. The factor $\sqrt{2}$ has been included to account for the fact that only a field $\mu_0 H/\sqrt{2}$ is applied per facet. The main I_c maximum in this normalization roughly appears at $N/2$. The dotted (blue) interference pattern is for $\Delta t_{\text{eff}} = 0$ to emphasize the “ideal” case. $\Delta t_{\text{eff}}/t_{\text{eff}0} = 0.02$ (black line) yields only minor deviations in the field range shown. The experimental curve is at an angle $\theta = -0.085^\circ$. No curve has been measured at $\theta = 0.0^\circ$ an angle, which is defined only after data analysis. Note that, in principle, the experimental and theoretical field scales are linked for a fixed value of f_{90} . However, in order to compare the *shape* of $I_c(H)$, in Fig. 5 (b) we have additionally compressed the experimental field scale by a factor of 1.2 to account for the nonzero value of θ . Further note that the experimental curve only covers a limited field range. This is the limit set by our experimental system. Comparing the curves at $\theta = 90^\circ$ and $\theta = 0^\circ$ one notices that for $\theta = 0^\circ$ the amplitudes of the secondary I_c maxima situated between the two main I_c maxima follow a U-shaped dependence while for $\theta = 90^\circ$ their amplitudes are about constant. Also, for $\theta = 0^\circ$ and absolute values of fields higher than the main I_c maxima, the I_c maxima are strongly reduced compared to $\theta = 90^\circ$. These are the main differences in $I_c(H)$ at $\theta = 0^\circ$ and $\theta = 90^\circ$. Thus, the overall difference of the interference pattern at $\theta = 90^\circ$ compared to the ideal case is much less striking than in previous publications²⁻⁵, presumably pointing to a much higher inhomogeneity of the critical current density in previous generations of ramp-zigzag $0-\pi$ JJs.

Fig. 6 compares measured and calculated interference patterns for $\phi = 45^\circ$ and $-1.128^\circ < \theta < 0.68^\circ$. In the experimental curves the offset angle $\theta_{\text{off}} = 1.684^\circ$ is not subtracted. The agreement is fair for all angles shown. The only additional parameter required to fit the whole series of curves was θ_{off} . It was determined by comparing the calculated interference pattern at the dead angle, cf. Fig. 6 (l), to the measured one, cf. Fig. 6 (k). For arbitrary ϕ , the dead angle $\theta_d \approx -\arctan[(\cos \phi + \sin \phi)/2f_{90}]$; $\theta_d \approx -0.4^\circ$ for $\phi = 45^\circ$. Near θ_d , variations in θ on the order of 0.01° already cause significant changes in I_c vs. H so that, once f_{90} is fixed, θ_{off} can be determined very precisely. Note that the experimental I_c vs. H pattern of Fig. 6 (k) slightly modulates around $2.5 \mu\text{A}$, while the calculated pattern in Fig. 6 (l) is almost at zero current. This is presumably caused by residual fields in the cryo-

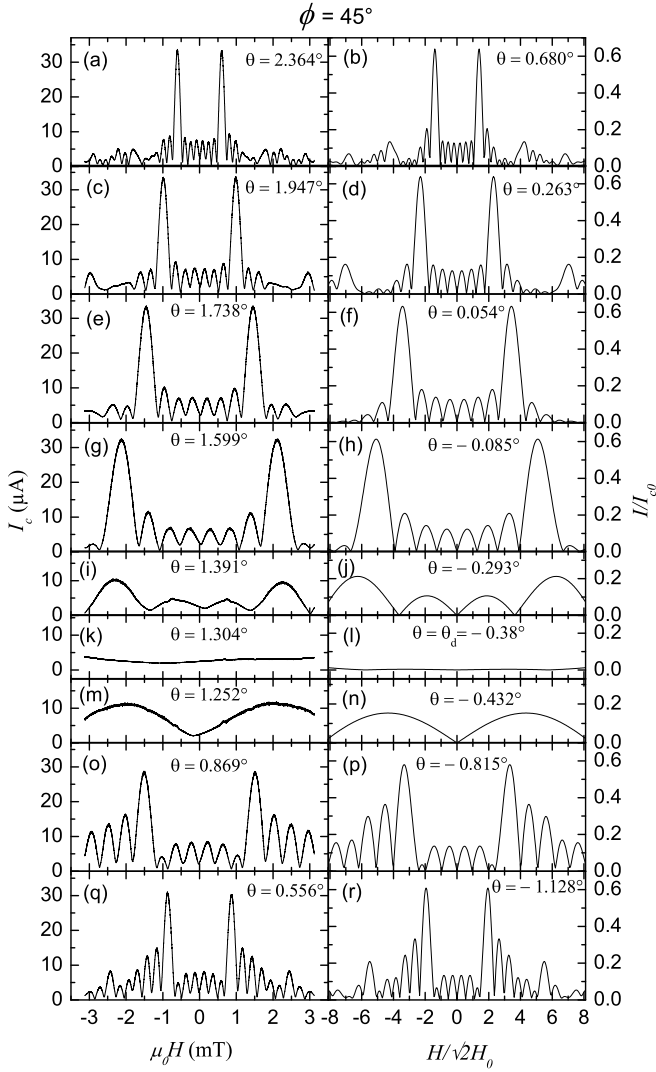


FIG. 6: Experimental (left) and calculated (right) interference patterns for $\phi = 45^\circ$ and $-1.128^\circ < \theta < 0.68^\circ$. Offset angle $\theta_{\text{off}} = 1.684^\circ$ is not subtracted in the experimental graphs. $H_0 = NLt_{\text{eff}0}/\Phi_0$. Critical current in the calculated plots is normalized to $I_{c0} = |j_c|A_J$, where j_c is the critical current density and A_J is the junction area. Model parameters are $\alpha_e = 0.5$, $a_{90,e} = 0.3$, $\alpha_f = 0.7$, $a_{90,f} = 2.0$, $f_{90} = 100$ and $\Delta t_{\text{eff}}/t_{\text{eff}0} = 0.02$.

stat, causing also the shift in the I_c minimum relative to $H = 0$ in Fig. 6 (m). Also, the θ dependence of the interference patterns strongly depends on f_{90} . This parameter cannot be altered by more than some 5% from 100 without substantial degradation of the fit quality.

To further confirm that the profile $B(\xi)$ – plus the assumption of homogeneous junction parameters – describes the situation well we have also varied ϕ . Fig. 7 compares data and calculations for $\phi = 0^\circ$ and various values of θ around $\theta = 0^\circ$. For the case of $\phi = \theta = 0^\circ$ calculations yield critical current main maxima $I_c = 0.5I_{c0}$ whenever the flux through the facets oriented along x equals a multiple of Φ_0 . Then the critical current of

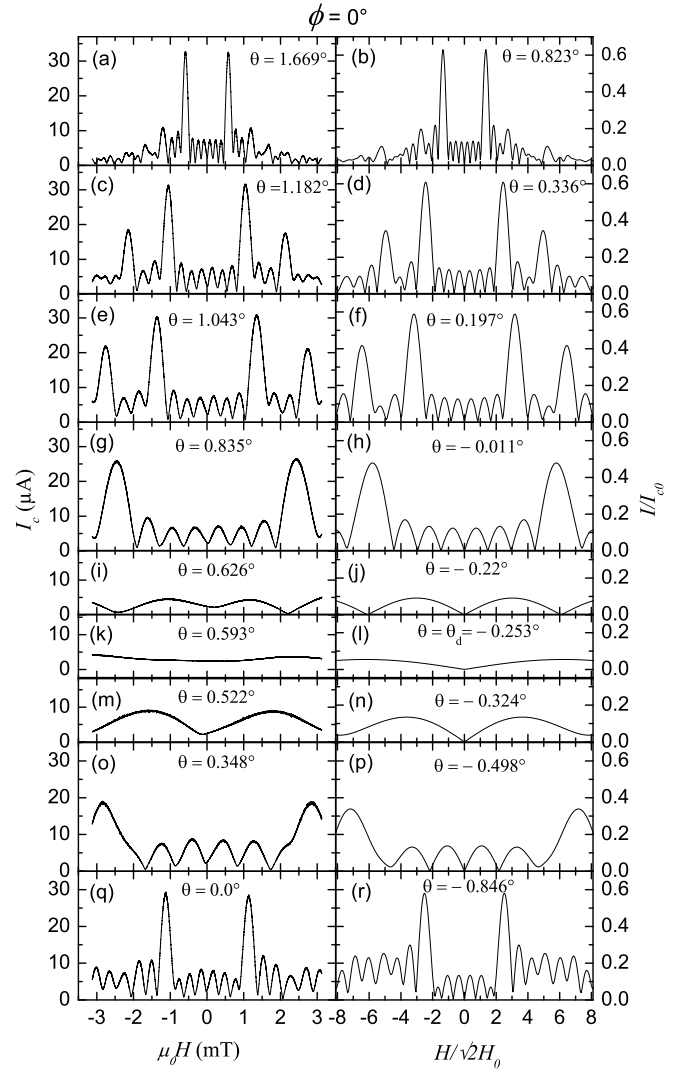


FIG. 7: Experimental (left) and calculated (right) interference patterns for $\phi = 0^\circ$ and $-0.846^\circ < \theta < 0.823^\circ$. Offset angle $\theta_{\text{off}} = 0.846^\circ$ is not subtracted in the experimental graphs. $H_0 = NLt_{\text{eff}0}/\Phi_0$. Critical current in the calculated plots is normalized to $I_{c0} = |j_c|A_J$, where j_c is the critical current density and A_J is the junction area. Model parameters are $\alpha_e = 0.5$, $a_{90,e} = 0.3$, $\alpha_f = 0.7$, $a_{90,f} = 2.0$, $f_{90} = 100$ and $\Delta t_{\text{eff}}/t_{\text{eff}0} = 0.02$.

these facets cancel and I_c is given by the sum of the critical currents of the facets oriented along y . Curves of Fig. 7 (a)–(f) show the appearance of the first and second main I_c maximum, which grows in amplitude for $\theta \rightarrow 0^\circ$. Although the maximum field provided by our setup was not sufficient to resolve the main maxima for $\theta = 0^\circ$ the evolution of the first and second I_c main peaks are clearly visible for $\theta < 0.336^\circ$, with a good agreement between experimental and theoretical patterns. By lowering θ one again runs through a dead angle ($\theta_d = -0.253^\circ$) and obtains somewhat strangely looking interference patterns for $-1^\circ < \theta < \theta_d$.

Finally, we address the effect of self fields generated by

the Josephson currents. Such effects become prominent when the junction is 2–3 times longer than the Josephson length λ_J . To estimate λ_J we first ignore idle regions and assume that the supercurrent flows homogeneously across the junction area $A_J = NLW \approx 37 \mu\text{m}^2$. We then find $j_{c0} = I_{c0}/A_J \approx 140 \text{ A/cm}^2$. Using $\lambda_{J0} = [\Phi_0/2\pi\mu_0 j_c d_{\text{eff}}]^{0.5}$, with the effective magnetic junction thickness³⁴ $d_{\text{eff}} = t_{\text{Au}} + \lambda_{\text{YBCO}} \coth(d_{\text{YBCO}}/\lambda_{\text{YBCO}}) + \lambda_{\text{Nb}} \coth(d_{\text{Nb}}/\lambda_{\text{Nb}}) \approx 470 \text{ nm}$, we find $\lambda_{J0} \approx 20 \mu\text{m}$ and the normalized junction length $l = NL/\lambda_J \approx 4$. The idle region effect^{36,37} leads to an increased Josephson length, $\lambda_{J,i} = \delta \cdot \lambda_{J0}$, with $\delta = (1 + (d_{\text{eff}}/d_{\text{eff},i})(W_i/W))^{0.5}$. W_i and $d_{\text{eff},i}$, respectively, are the width and effective magnetic thickness of the idle region. With $d_{\text{eff},i} = 535 \text{ nm}$ and $W_i = 3 \mu\text{m}$ one obtains $\delta \approx 2.6$ and $\lambda_{J,i} \approx 50 \mu\text{m}$. Thus, $l \approx 1.6$, justifying the short junction approach taken above. An ambiguity, however, arises from the problem to refer the measured I_c to the proper junction area. Above, we have used the whole ramp area. Alternatively, assuming that the current is dominantly carried by the in-plane currents on the YBCO side one might refer to a junction area which is projected perpendicular to the substrate plane. Then, j_c increases by a factor of 7 and λ_J decreases by a factor of 3, bringing the junction closer to the long junction regime. To distinguish these scenarios we simulated $I_c(H)$ based on the sine-Gordon equations for the case of $\theta = 90^\circ$ and various values of the normalized junction length l . Fig. 8 shows simulations of $I_c(H)$ patterns for different l and the calculation using the short junction model. Deviations from the short junction model that are incompatible with our experimental data become prominent near the main I_c maxima for $l > 3$ (the case of $l = 4$ is shown in the graph). By contrast, $I_c(H)$ for $l = 1.6$ is almost indistinguishable from the short junction model and in agreement with the above estimate, using the ramp area instead of its projection.

E. Conclusions

In summary, we have investigated the interference patterns I_c vs. H for a 8 facet YBCO-Au-Nb zigzag-ramp Josephson junction, with a facet length of $10 \mu\text{m}$. The angle θ between the substrate plane and the applied field H was systematically varied and we also discussed two in-plane angles ϕ between H and the facet orientation (0° and 45°). All interference patterns could be understood from the fact that a field component perpendicular to the substrate causes a strong and spatially varying contribution to the flux density profile inside the junction. The junction by itself – admittedly our best junction – seems to be very homogeneous, with an essentially constant critical current density inside each facet. Particularly, no j_c asymmetry between facets oriented along the in-plane x and y directions were observable. We have expected a strong dephasing effect on I_c vs. H due to the fact that the flux penetrating the junction is not preserved.

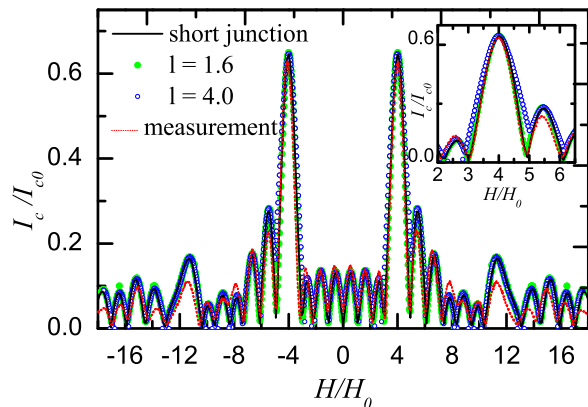


FIG. 8: (Color online). I_c vs. H ($\theta = 90^\circ$) patterns calculated with the short junction model for $\Delta t_{\text{eff}} = 0$ (solid line) and simulated for different lengths l (circles) using StkJJ³⁸ in comparison with measurement (dotted line). Deviations between the calculated and the simulated (for $l = 4$) pattern are visible in the zoomed inset.

The effect is present but at least an order of magnitude weaker than expected. Our investigations also showed that H is applied “parallel” to the junction (in terms of an homogeneous flux density profile) for $\theta \approx 0^\circ$ and not for a field orientation about parallel to the ramp angle $\theta_r = 8^\circ$. These findings may contribute new knowledge to the general physics of ramp junctions.

Further, due to strong compression of the perpendicular field component by about a factor of 100 only for angles $|\theta| \ll 0.1^\circ$ the interference patterns were “ideal” in the sense that the flux density in the junction is essentially homogeneous. The effective junction thickness is only about 85 nm, leading to enormous fields ($\sim 35 \text{ mT}$) that are required to produce a flux quantum per $(0 - \pi)$ -segment for the case of $\theta = 0^\circ$. We also demonstrated, that there is a dead angle very close to “parallel” field orientation, where tremendous changes in $I_c(H)$ occur. These properties make it extremely hard to study zigzag junctions in “parallel” field configuration. Due to idle regions the Josephson length of our junction was on the order of $50 \mu\text{m}$, requiring junction lengths of several $100 \mu\text{m}$ to study long junction effects. For such junctions the field compression will be even bigger than in our case, and, thus, the field alignment must be better than 0.01° to achieve a homogeneous flux density. Thus it seems that, for a study of (semi)fluxon physics^{3,6,7,12} or φ -junction effects^{15–18} in zigzag junctions magnetic fields should be oriented perpendicular to the substrate plane and the corresponding flux density profiles should be taken into account rather than being avoided by parallel field alignment.

Acknowledgments

We acknowledge financial support by the Deutsche Forschungsgemeinschaft (Project KO 1303/10) and by

the German Israeli Foundation (Grant No. G-967-126.14/2007).

-
- * Electronic address: kleiner@uni-tuebingen.de
- ¹ D. J. van Harlingen, *Rev. Mod. Phys.* **67**, 515 (1995).
 - ² H.-J. H. Smilde, Ariando, D. H. A. Blank, G. J. Gerritsma, H. Hilgenkamp, and H. Rogalla, *Phys. Rev. Lett.* **88**, 057004 (2002).
 - ³ H. Hilgenkamp, Ariando, H. H. Smilde, D. H. A. Blank, G. Rijnders, H. Rogalla, J. Kirtley, and C. C. Tsuei, *Nature (London)* **422**, 50 (2003).
 - ⁴ C. Gürlich, E. Goldobin, R. Straub, D. Doenitz, Ariando, H.-J. H. Smilde, H. Hilgenkamp, R. Kleiner, and D. Koelle, *Phys. Rev. Lett.* **103**, 067011 (2009).
 - ⁵ Ariando, D. Darminto, H. J. H. Smilde, V. Leca, D. H. A. Blank, H. Rogalla, and H. Hilgenkamp, *Phys. Rev. Lett.* **94**, 167001 (2005).
 - ⁶ K. Cedergren, J. R. Kirtley, T. Bauch, G. Rotoli, A. Troeman, H. Hilgenkamp, F. Tafuri, and F. Lombardi, *Phys. Rev. Lett.* **104**, 177003 (2010).
 - ⁷ K. Cedergren, T. Bauch, H. Pettersson, J. R. Kirtley, E. Olsson, and F. Lombardi, *Supercond. Sci. Technol.* **23**, 034027 (2010).
 - ⁸ M. Weides, M. Kemmler, H. Kohlstedt, R. Waser, D. Koelle, R. Kleiner, and E. Goldobin, *Phys. Rev. Lett.* **97**, 247001 (2006).
 - ⁹ M. Weides, C. Schindler, and H. Kohlstedt, *J. Appl. Phys.* **101**, 063902 (2007).
 - ¹⁰ G. Wild, C. Probst, A. Marx, and R. Gross, *Eur. Phys. J. B* **78**, 509 (2010), ISSN 1434-6028.
 - ¹¹ C. C. Tsuei and J. R. Kirtley, *Rev. Mod. Phys.* **72**, 969 (2000).
 - ¹² H. Susanto, E. Goldobin, D. Koelle, R. Kleiner, and S. A. van Gils, *Phys. Rev. B* **71**, 174510 (2005).
 - ¹³ A. Buzdin, *Phys. Rev. Lett.* **101**, 107005 (2008).
 - ¹⁴ A. Gumann and N. Schopohl, *Phys. Rev. B* **79**, 144505 (2009).
 - ¹⁵ A. Buzdin and A. E. Koshelev, *Phys. Rev. B* **67**, 220504 (2003).
 - ¹⁶ E. Goldobin, D. Koelle, R. Kleiner, and A. Buzdin, *Phys. Rev. B* **76**, 224523 (2007).
 - ¹⁷ A. Zazunov, R. Egger, T. Jonckheere, and T. Martin, *Phys. Rev. Lett.* **103**, 147004 (2009).
 - ¹⁸ E. Goldobin, D. Koelle, R. Kleiner, and R. G. Mints, *Phys. Rev. Lett.* **107**, 227001 (2011).
 - ¹⁹ R. G. Mints, *Phys. Rev. B* **57**, R3221 (1998).
 - ²⁰ R. G. Mints and I. Papiashvili, *Phys. Rev. B* **64**, 134501 (2001).
 - ²¹ R. G. Mints, I. Papiashvili, J. R. Kirtley, H. Hilgenkamp, G. Hammerl, and J. Mannhart, *Phys. Rev. Lett.* **89**, 067004 (2002).
 - ²² M. Moshe and R. G. Mints, *Phys. Rev. B* **76**, 140507 (2007).
 - ²³ T. Ortлеpp, Ariando, O. Mielke, C. J. M. Verwijs, K. F. K. Foo, H. Rogalla, F. H. Uhlmann, and H. Hilgenkamp, *Science* **312**, 1495 (2006).
 - ²⁴ J. Oppenländer, C. Häussler, T. Träuble, P. Caputo, J. Tomes, A. Friesch, and N. Schopohl, *IEEE Trans. Appl. Supercond.* **13**, 1051 (2003).
 - ²⁵ M. Seifried, C. Häussler, J. Oppenländer, and N. Schopohl, *IEEE Trans. Appl. Supercond.* **15**, 781 (2005).
 - ²⁶ R. Monaco, M. Aaroe, J. Mygind, and V. P. Koshelets, *J. Appl. Phys.* **104**, 023906 (2008).
 - ²⁷ R. Monaco, M. Aaroe, J. Mygind, and V. P. Koshelets, *Phys. Rev. B* **79**, 144521 (2009).
 - ²⁸ M. Moshe, V. G. Kogan, and R. G. Mints, *Phys. Rev. B* **79**, 024505 (2009).
 - ²⁹ S. Scharinger, C. Gürlich, R. G. Mints, M. Weides, H. Kohlstedt, E. Goldobin, D. Koelle, and R. Kleiner, *Phys. Rev. B* **81**, 174535 (2010).
 - ³⁰ R. De Luca, *Supercond. Sci. Technol.* **24**, 065026 (2011).
 - ³¹ C. Gürlich, S. Scharinger, M. Weides, H. Kohlstedt, R. G. Mints, E. Goldobin, D. Koelle, and R. Kleiner, *Phys. Rev. B* **81**, 094502 (2010).
 - ³² J. K. Heinsohn, R. Dittman, J. R. Contreras, E. Goldobin, A. M. Klushin, and M. Siegel, *J. Appl. Phys.* **90**, 4623 (2001).
 - ³³ H.-J. H. Smilde, H. Hilgenkamp, G. Rijnders, H. Rogalla, and D. H. A. Blank, *Appl. Phys. Lett.* **80**, 4579 (2002).
 - ³⁴ M. Weihnacht, *Phys. Stat. Sol.* **32**, 169 (1969).
 - ³⁵ M. Khapaev, M. Kupriyanov, E. Goldobin, and M. Siegel, *Supercond. Sci. Technol.* **16**, 24 (2003).
 - ³⁶ R. Monaco, G. Costabile, and N. Martucciello, *J. Appl. Phys.* **77**, 2073 (1995).
 - ³⁷ S. Maggi and V. Lacquanti, *J. Low Temp. Phys.* **106**, 393 (1997).
 - ³⁸ E. Goldobin, STKJJ – USER’S REFERENCE (2011), URL <http://www.geocities.com/SiliconValley/Heights/7318/StkJJ.htm>